NGSO-To-GSO Satellite Interference Detection Based on Autoencoder

Almoatssimbillah Saifaldawla, Flor G. Ortiz-Gomez, Eva Lagunas, Saed Daoud and Symeon Chatzinotas
Interdisciplinary Centre for Security Reliability and Trust (SnT),
University of Luxembourg, Luxembourg
e-mail: {moatssim.saifaldawla, flor.ortiz, eva.lagunas, saed.daoud, symeon.chatzinotas}@uni.lu

***Abstract*—Recently, non-geostationary orbit (NGSO) satellite communication constellations have regained popularity due to their ability to provide global coverage and lower-latency connectivity. However, the new wave of Low Earth Orbit (LEO) satellite constellations operate on the same spectral bands as legacy satellites in geosynchronous orbit (GSO), which concurrently access the electromagnetic spectrum. Even if international regulations are in place, such increased spectral congestion will result in interference events. Therefore, both regulator entities and GSO operators have a high interest in detecting illegal or unlicensed NGSO interference sources. In this work, we simulate a realistic downlink interference scenario by emulating an actual commercial NGSO orbit whose signal is eventually received in a GSO receiver that is pointed toward a specific GSO satellite. We design an autoencoder deep neural network and we evaluate its performance considering both time-series and frequency-domain series of the overall received samples. Extensive numerical results are presented, validating the interference detection accuracy and comparing both domains of inputs at the autoencoder.**

***Index Terms*—NGSO, GSO, Spectrum Sharing, Interference Detection, Deep Learning, Autoencoder**

I. Introduction

An increasingly large number of non-geostationary orbit (NGSO) satellites have been or are set to be deployed in space to provide ubiquitous internet access with relatively low propagation delay. A clear example of such trends are the mega-constellation satellite networks of SpaceX, OneWeb, and Amazon [1].

The new wave of Low Earth Orbit (LEO) satellite constellation is expected to operate in Ku-Ka bands, where legacy geostationary satellite orbit (GSO) systems have been operating for decades. While national and international regulators are working hard to establish fair and equitable treatment for all space actors, there is a growing concern about how such massive small satellite mesh networks will affect the operations of GSO systems [2]. Therefore, the coexistence of these networks in terms of spectrum sharing needs to be thoroughly examined and analyzed.

Signal interference adversely affects the communication channel, which leads to degradation of Quality of Service (QoS), reduced operational efficiency, and eventually revenue loss [3]. Thus, many researchers in the literature have been addressing spectrum sharing and the entailed interference management issues, specifically the interference between GSO-NGSO satellites [4], [5], [6], [7]. These papers are based on conventional interference analysis techniques e.g., Power Spectral Density (PSD) analysis. However, it can be time-consuming, costly, and challenging, particularly against unknown or novel interference types or when there are interfering signals with minor Signal-to-noise ratio (SNR) power hidden within the noise floor. As a consequence, conventional methods show weaknesses in practical scenarios. Integrating Artificial Intelligence (AI) into interference detection can bring advanced capabilities that can significantly enhance the effectiveness and efficiency of satellite communication system monitoring and interference mitigation [8], [9].

Data-driven approaches that employ Deep learning (DL) algorithms have been considered in [10], where the interference classification problem is studied for satellite systems. In particular, signal classification is performed by directly processing the IQ samples. While the incumbent signal is a GSO downlink signal, the interference is assumed to be from a terrestrial cellular system. The authors in [11] presented another DL approach to automatically detect short- and long-term interference in the NGSO signal spectrum received at the satellite ground station. Therefore, [11] considers the NGSO as the primary signal and aims at detecting interference/jamming, which is artificially generated and manually introduced to the NGSO communication signal.

In an attempt to shed light into a relevant scenario such that of the NGSO-GSO spectrum coexistence, in this work we focus on a reference scenario where the legacy system is the GSO downlink. Such GSO link is eventually interfered by a NGSO orbit with a low angular separation from their line-of-sight downlink. In this context, we develop an autoencoder deep-learning model for the purpose of detecting interference from the NGSO satellite's -specifically a LEO satellite- downlink paths towards a GSO's user terminal (UT). The main idea of this article is to introduce a method for interference detection (which serves as the initial stride toward mitigating and suppressing interference) by utilizing a deep-learning approach based on autoencoders. Real-time trajectory and positions of co-existing NGSO and GSO satellites are simulated using their Two-line elements (TLE) information [12]. The contribution of our work can be summarized in the next points:

- We simulate a realistic downlink interference scenario where a GSO UT is receiving a primary signal from

This work is financially supported by the Luxembourg National Research Fund (FNR) under the project SmartSpace (C21/IS/16193290).

a GSO satellite and it is eventually interfered by a NGSO downlink (depending on the geometry of the orbit propagation and pointing angles).
- Accurate satellites' link budget calculations using actual system parameters is performed while considering the GSO's UT off-axis angle (which affects the receive antenna gain), and the dynamics depending on the NGSO satellite movement.
- An autoencoder deep-learning model is proposed to detect the interference in the received signals in both the time and frequency domains.
- Finally, we provide a comparison of the interference detection accuracy of the model over time and frequency domain data and discuss which data representation is more efficient in detecting the interference.

The remainder of the paper is organized as follows: Section II describes the system model regarding the link budget calculation and the digital baseband received signal model. Section III describes the Scenario simulation, training data generation, and the DL-based approach. Section IV presents the experimental results. Finally, Section V concludes the paper.

II. System Model

This work analyzes the downlink scenario of forward links of two co-existing satellite communication systems. A desired primary GSO satellite system, and a LEO satellite as a secondary system and source of interference to GSO's user terminals (UTs).

A. Link Budget Calculation

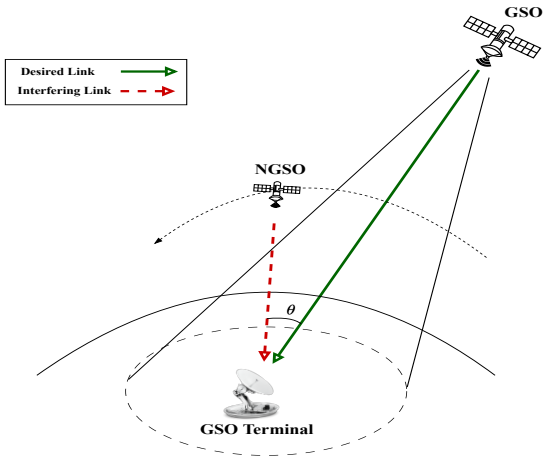

Fig. 1. Desired and interference links of GSO and NGSO Systems

In this downlink scenario, we are assuming that the GSO and LEO Satellites are sending their signal while the transmission main lobe always pointing toward a GSO user terminal (UT) as illustrated in Fig. 1.

The carrier-to-noise ratio (C/N) from the GSO satellite at the UT can be formulated as

$$C/N = \frac{P_{tg} G_{tg} G_{rg}(\theta_0)/(4\pi d_g/\lambda_g)^2}{\kappa Tem B_{noise}} \quad (1)$$

where P_{tg} is the transmit power of the desired GSO satellite antenna, Gtg, and $Gr_g(\theta_0)$ denote the gains of the GSO satellite antenna and UT receiver, respectively, θ_0 is the off-axis angle between the receiver main lobe axes and the GSO communication link, the term $(4\pi d_g/\lambda_g)^2$ gives the Free space path loss (FSPL) in the link, in which d_g is the slant range between the GSO satellite and the user, and the wavelength of the carrier signal λ_g is related to the light speed c and GSO's carrier frequency f_g by the relationship $\lambda = c/f_g$. Tem is the receiver's noise temperature, κ represents the Boltzmann constant, and B_{noise} is the noise bandwidth.

The UT is fixed on the ground and maintains a constant pointing direction towards its corresponding GSO satellite, in order to achieve maximum gain from the receiving antenna. Thus, θ_0 is set to zero when calculating the desired C/N. While the LEO satellite is moving in visible positions to the UT, the user then might also receive the LEO signals when they are carried in the same frequency band. These LEO signals would primarily increase the level of interference in the signal. The downlink interference-to-noise ratio (I/N) received by the GSO's UT from the interfering LEO satellite antenna beam can be calculated as

$$I/N = \frac{P_{tl} G_{tl} G_{rl}(\theta_l)/(4\pi d_l/\lambda_l)^2}{\kappa Tem B_{noise}} \quad (2)$$

where P_{tl} is the transmit power of the LEO satellite antenna, G_{tl} is the gain of the LEO satellite antenna, d_l is the slant range between the interfering satellite and the GSO user terminal,θ_l represents the off-axis angle between the receiver main lobe axes and the LEO communication link, and the wavelength of the carrier signal λ_l is related to the light speed c and LEO's carrier frequency f_l by the relationship $\lambda_l = c/f_l$. The worst-case scenario where the LEO is In-line with the GSO's line-of-sight(LOS) path toward the UT, generally, only happened when ($\theta_l = \theta_0 = 0$), but in our analysis, we will assume that our worst-case is when we had ($\theta_l \approx \theta_0$). This in-line scenario will result in the I/N being in its peak values because we will have ($Gr_l \approx Gr_g$). We also consider the carrier-to-interference plus noise ratio $C/(I+N)$ or ($CINR$) interference evaluation metric to determine the level of interference caused by the LEO satellite on the GSO system. Most importantly, the computation of the off-axis angle between the user and the LEO's beam direction is following the law of cosine

$$\theta_l = \arccos\left(\frac{d_g^2 + d_l^2 - d_{gl}}{2 d_g d_l}\right) \quad (3)$$

d_{gn} is the slant range between the GSO and LEO satellite. While considering the maximum transmitting gain from GSO and LEO satellites, the received gain is critical in our scenario. Due to the LEO satellite movement, the received gain varies with the satellite movement, it thus is determined according

to the LEO satellite off-axis angle as seen from the UT. For simplicity, we are applying a general radiation pattern for a very small-aperture terminal (VSAT) parabolic dish received gain Gr, and it is related to the first-order Bessel function J_1 [13] as

$$Gr(\theta) = Gr(\theta_0)\left[\frac{2\lambda}{\pi D_A}\frac{J_1\left[(\pi D_A/\lambda)sin(\theta)\right]}{sin(\theta)}\right] \quad (4)$$

where D_A is the diameter of the receiver antenna's aperture in meters, λ is the wavelength in meters, θ is the off-axis angle in degrees from the antenna's symmetry axis here $\theta \equiv \theta_l$; $Gr(\theta_0)$ can be obtained from the first nulls of the radiation pattern, it represents the maximum gain at beamwidth θ_0, and $Gr(\theta_0) = e_A\left[\frac{\pi D_A}{\lambda}\right]^2$ where e_A is the receiver aperture efficiency.

B. Baseband Received Signal Model

In the downlink of the GSO system Forward link (FWD), a GSO satellite is transmitting the baseband signal $x(t)$ (henceforth called the desired signal) to the UT receiver, which is given as

$$x(t) = \sum_{k=0}^{K-1} x[k]p_X(t - kT_X), \quad t \in [0, KT_X] \quad (5)$$

where $x[k]_{k=0}^{K-1}$ are the modulated symbols depending on the MODCOD used for DVB-S2X standard, each with average power P_X and duration T_X, $p_X(t)$ is a rectangular pulse shaping filter of duration T_X and unit energy, T_X is related to the baseband bandwidth of the signal B_x as $T_X = 1/B_x$, and K is the number of symbols in the desired signal block. The spectrum ranges $[f_{gmin}, f_{gmax}]$ is assumed to be allocated for the GSO satellite system, which is divided into some subbands, each of bandwidth $2B_x$, and each subband has a center frequency. The carrier frequency of the desired signal f_g can assume any of these center frequencies and subbands. At the same time, the LEO satellite system may transmit the baseband signal $i(t)$ (henceforth called the interference signal) of length N that may interfere with $x(t)$ at the GSO's user UT, which is given as

$$i(t) = \sum_{\nu=0}^{V-1} i[m]p_I(t - \nu T_I), \quad t \in [0, VT_I] \quad (6)$$

where $i[\nu]_{\nu=0}^{V-1}$ are modulated symbols depending on the MODCOD specified by LEO's system, each of average power P_I and duration T_I, which is related to the baseband bandwidth B_i as $T_I = 1/B_i$, $p_I(t)$ is a rectangular pulse shaping filter of duration T_I and unit energy. For simplicity, We assume that $VT_I = KT_X$, i.e., both the desired and interference signal blocks have the same total time duration. Furthermore, we are assuming Binary Phase shift keying (BPSK) MODCOD for both $x(t)$ and $i(t)$ signals. The spectrum ranges $[f_{lmin}, f_{lmax}]$ is assumed to be allocated for the LEO satellite system, which is divided into some subbands, each of bandwidth B_i, each subband has a center frequency. The frequency of the interfering signal f_l is assumed to be sent in the same GSO's center carrier frequency for now. At UT, the baseband received signal can be expressed in the time domain after down-converting the bandpass received signal by f_g as

$$r(t) = x(t)\sqrt{C/N} + \alpha i(t)\exp^{j2\pi(f_l - f_g)t}\sqrt{I/N} + \zeta(t) \quad (7)$$

In this equation, C/N and I/N represent the SNR of the desired signal x(t) and interference signal i(t), respectively. $\zeta(t)$ is complex-valued additive white Gaussian noise (AWGN) process of zero-mean and unity power over the bandwidth $2B_x$. The variable α indicator for interference signal $i(t)$ appearances [1], when the LEO satellite is not visible to the user there is no interference (received signals without interference) $\alpha = 0$, and when the LEO satellite is visible and actively sending interference signal to the user(received signals with interference) $\alpha = 1$.

III. Interference Detection Model

We selected one GSO satellite from SES fleet, the ASTRA19.2 system, and one LEO satellite from SpaceX's STARLINK constellation. ASTRA 19.2 is a European broadcasting satellite (ITU Region 1). The Ku band in this region corresponds to 10.7 - 12.7 GHz for direct broadcast satellite services (DBSS) such as those carried by the ASTRA satellites [14]. On the other hand, STARLINK constellations are deployed to provide broadband connectivity worldwide, which is part of the Fixed Satellite Services (FSS). According to SpaceX's recent filings with the Federal Communications Commission (FCC), STARLINK satellites operate in the Ku frequency bands 10.7–12.7 GHz [15].

A. Scenario Generation

The ASTRA and STARLINK satellite's real-time position and trajectory information is based on Kepler's six orbital elements, which can be easily extracted from the corresponding satellite's Two-line elements (TLE) information [12]. From ASTRA 19.2 system, we chose the "ASTRA 1N"; while from the STARLINK system, we selected the "STARLINK-2737" as the LEO satellite. The corresponding orbit propagation of the selected NGSO satellite has been calculated with MATLAB toolbox, which provides the estimates of latitude, longitude, and altitude over time accordingly to the satellite trajectory. The UT is assumed to be a VSAT dish located in our research center's "SnT" building in Luxembourg City, Luxembourg. To generate the data for our model, we recorded a sample of the signals every 10 seconds, referred to as a Time-sample $\mathcal{T}_n$, n = 1, 2, ..., $\mathcal{N}$.

Table I shows the access intervals of both LEO and GEO satellites to the user terminal. It can be observed that the ASTRA 19.2 satellite has continuous access to the UT all the time with a total duration of 24 hours (86400 seconds), while the STARLINK satellite has discrete access to the UT,

[1]UT only receives interference power from LEO, the noise power is added at the front-end receiver

TABLE I
THE ACCESS TABLE OF GSO, NGSO TO THE UT

Source	Target	IntervalNumber	StartTime	EndTime	Duration (sec)
"ASTRA1N"	"SnT"	1	20-Mar-2023 00:00:00	21-Mar-2023 00:00:00	86400
"STARLINK-2737"	"SnT"	1	20-Mar-2023 08:54:30	20-Mar-2023 09:01:30	420
"STARLINK-2737"	"SnT"	2	20-Mar-2023 10:30:30	20-Mar-2023 10:42:30	720
"STARLINK-2737"	"SnT"	3	20-Mar-2023 12:09:30	20-Mar-2023 12:22:10	760
"STARLINK-2737"	"SnT"	4	20-Mar-2023 13:49:30	20-Mar-2023 14:02:00	750
"STARLINK-2737"	"SnT"	5	20-Mar-2023 15:29:20	20-Mar-2023 15:42:00	760
"STARLINK-2737"	"SnT"	6	20-Mar-2023 17:09:10	20-Mar-2023 17:21:00	710
"STARLINK-2737"	"SnT"	7	20-Mar-2023 18:50:00	20-Mar-2023 18:57:00	420

TABLE II
LINKS PARAMETERS AND LINKS BUDGET CALCULATED VALUES AS OF 10:35:40 ON 20-MAR-2023

Parameter	*Value*
ASTRA satellite Parameters	
Satellite [lat, lon]	[-0.0048°,19.2328°]
Satellite alt	35764.08 Km
Distance to the user d_g	38427.14 km
Transmitted Power P_{tg}	15 dB
Transmitted Gain G_{tg}	42.9 dB
Channel bandwidth B_x	250 MHz
Frequency band $[f_{gmin} - f_{gmax}]$	[10.7 - 12.7] GHz
Center of the carrier frequency f_g	11.825 GHz
The free-space path loss (FSPL)	205.59 dB
STARLINK satellite Parameters	
Satellite [lat, lon]*	[142.4117°,9.8403°]
Satellite alt*	554.77 km
Distance to the user d_l*	1045.50 km
Transmitted Power P_{tl}	10 dB
Transmitted Gain G_{tl}	30 dB
Channel bandwidth B_i	250 MHz
Frequency band $[f_{lmin} - f_{lmax}]$	[10.7 - 12.7] GHz
Center of the carrier frequency f_l	11.825 GHz
The free-space path loss (FSPL)	174.29 dB
ASTRA UT Parameters	
UT [lat, lon]	[49.6257°,6.1598°]
UT alt	300 m
Antenna diameter D_A	0.9 m
Antenna efficiency e_A	0.6
Wavelength λ	0.0254 m
Noise Bandwidth B_{noise}	250 MHz
Receiver Noise temperature Tem	250° K
Maximum Rx antenna gain	38.73 dB
ASTRA link received antenna gain G_{rg}	38.73 dB
STARLINK link received Off_ axis angle θ_l*	4.9854°
STARLINK link received antenna gain G_{rl}*	26.28 dB
Effective gain-to-noise-temperature ratio (G/T)	14.74 dB
Received C/N	11.67 dB
Received I/N*	12.83 dB
Corresponding $CINR$*	-1.38 dB

* These values vary with the STARLINK satellite changing positions, for each other simulation Time-sample ($\mathcal{T}_n$) in the Time-frame ($\vec{\mathcal{T}_\mathcal{N}}$)

occurring 7 times during the whole time period, with varying access duration (420 to 720 seconds).

Fig. 2 illustrates the received signals' quality scenario by taking the second STARLINK Interval [20-Mar-2023 10:30:30 to 20-Mar-2023 10:42:30]. As can be seen in the figure, the worst case is when I/N is the highest, which gives the worst $CINR$, in this Interval, this happens when the **Simulation**

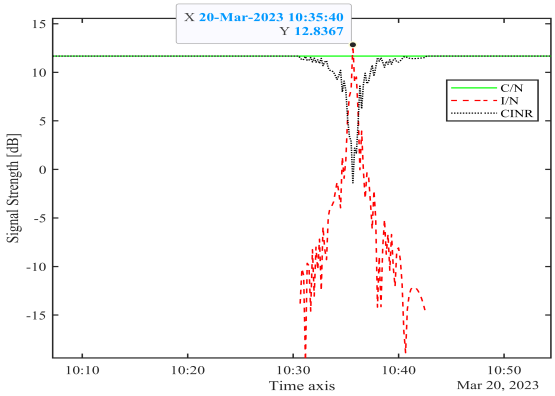

Fig. 2. Illustration of the received signals quality at UT in second STARLINK Interval

Time-sample $\mathcal{T}_n \cong$ 10:35:40 on 20-Mar-2023. Moreover, the interference does not exist when the STARLINK satellite has no visible access to the user, thus I/N does not appear in Fig. 2 and it is only depicted within its access intervals as detailed in Table I.

For each n-th simulation Time-sample, the $C/N^{(n)}$, $I/N^{(n)}$, and $CINR^{(n)}$ are calculated. A summary of the overall simulation parameters is described in Table II.

B. Data Generation

The link budget parameters detailed in the previous section are used to obtain raw data samples in time domain based on (7), and later transformed to the frequency domain.

In particular, we generate the baseband received signals using BPSK modulation with 2 GHz sampling frequency f_s, Jx = ceil(f_s/B_x) samples per $x[K]$ symbol, and 10 symbols per $x(t)$ signal, thus the number of samples per signal or the signal length S_{Time} = **80** components represents the amplitude of the signals and the same values for $i(t)$. Once the time domain signal in (7) is obtained, the Power Spectrum Density (PSD) is derived using the Welch method [16]. With a frequency window size of 1 GHz, eventually, we get S_{PSD} = **81** components representing the PSD's values in dB, which is convenient to later compare the performance of the proposed model for both data representations.

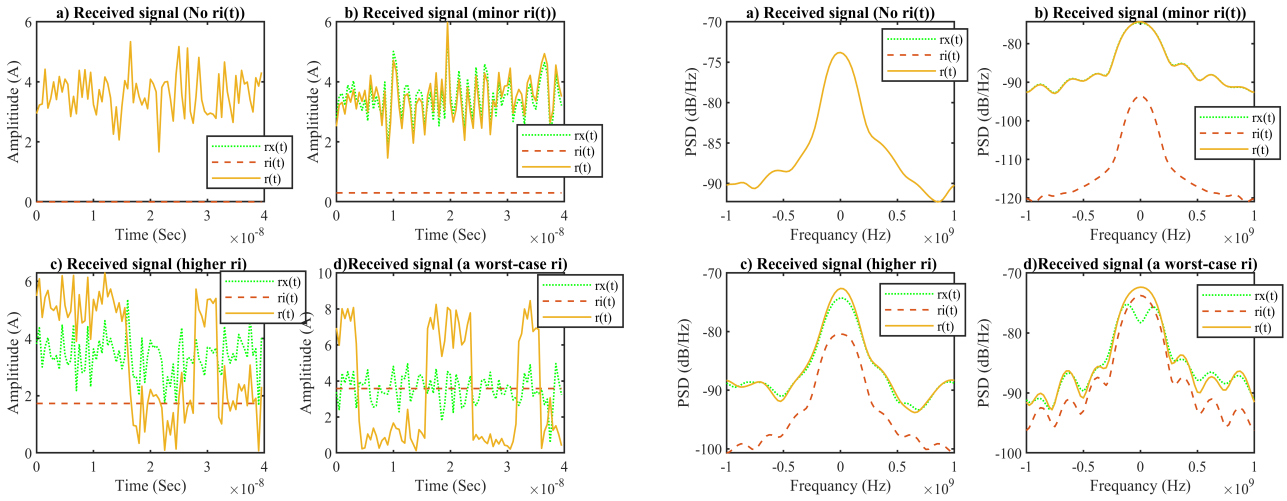

Fig. 3. Examples of different Generated Scenarios of the received ComplexTime signals in absolute and their Power Spectrum Density (PSD) representations (**rx(t)** represents the desired GSO signal, **ri(t)** represents the NGSO interference SIGNAL POWER, and **r(t)** depicts the actual received signal at the UT receiver).

It is worth noting that the presence of interference in a particular time instant (i.e. variable $\alpha^{(n)}$) is determined by the geometry of the scenario. In other words, $\alpha^{(n)} = 0$ when the STARLINK satellite is out of the field of vision of the user terminal.

As examples, Fig. 3 illustrates different interference scenarios generated based on the proposed NGSO orbit propagation. These scenarios include (a) the scenario where there is no interference signal, (b) the scenario where there is a negligible interference value, but it still exists, (c) the case with a smaller interference signal value, and (d) the worst-case scenario where the LEO satellite is on the most interfering position.

We finally obtain the actual received signal vector $\vec{r}_{\mathcal{M}}^{(n)}$ which represents the signal $r^{(n)}(t)$ components or its corresponding PSD values at the n-th simulation Time-sample, n= 1,2,...,$\mathcal{N}$ and $\mathcal{M} \in \{S_{Time}, S_{PSD}\}$. Thus, we will generate two matrices, both matrices contain $\mathcal{N}$ = **8641** signal samples (rows), and each sample has $\mathcal{M}$ signal component (column). The matrices will be notated as

- TimeSignals matrix $r_{Time} \in \mathbb{R}^{\mathcal{N}\times\mathcal{M}}$, $\mathcal{M} = S_{Time}$.
- PSD matrix $r_{PSD} \in \mathbb{R}^{\mathcal{N}\times\mathcal{M}}$, $\mathcal{M} = S_{PSD}$.

For training our model, we will require interference-free data. Therefore, we split the data into a training dataset (only including interference-free data) and a testing dataset (including both interference-free and non-interference-free data). We make use of the binary indicator $\alpha_{\mathcal{N}}^{\rightarrow} \in \{0, 1\}$ from (7) as splitting label:

- When $\alpha^{(n)} = 0$, we have a Normal_data segment (Interference-free Signal).
- When $\alpha^{(n)} = 1$, we have an Anomalous_data segment (Non-interference-free Signal).

The **8641** data contains **8181** interference-free signals and **460** signals effected with interference, with the help of $\alpha_{\mathcal{N}}^{\rightarrow}$, we split the total data as follows:

- **80%** of the Normal_data segments (**6536** Inputs) as **Train_data** set .
- The reminder **20%** of the Normal_data segments (**1645** Inputs) + **100%** of the Anomalous_data segments(**460** Inputs) as **Test_data** set.

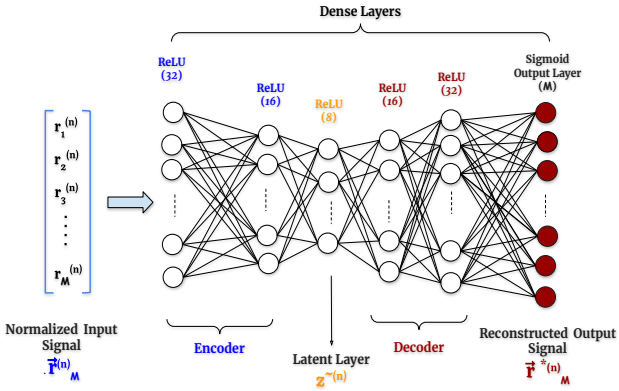

Fig. 4. Illustration of an autoencoder model architecture

C. Proposed DL approach

We propose an unsupervised learning approach based on the Autoencoders model (AEs) [17] for interference detection. This Autoencoder model uses "Encoder" layers to encode or compress the original signal $\vec{r}_{\mathcal{M}}^{(n)}$ into a latent-space representation and "Decoder" layers to decode or reconstructs the encoded data (latent space representation) back to the original dimension and produce $\vec{r^*}_{\mathcal{M}}^{(n)}$. The architecture of the Autoencoder model is described in Fig.4. The autoencoder model can be represented by the following equations

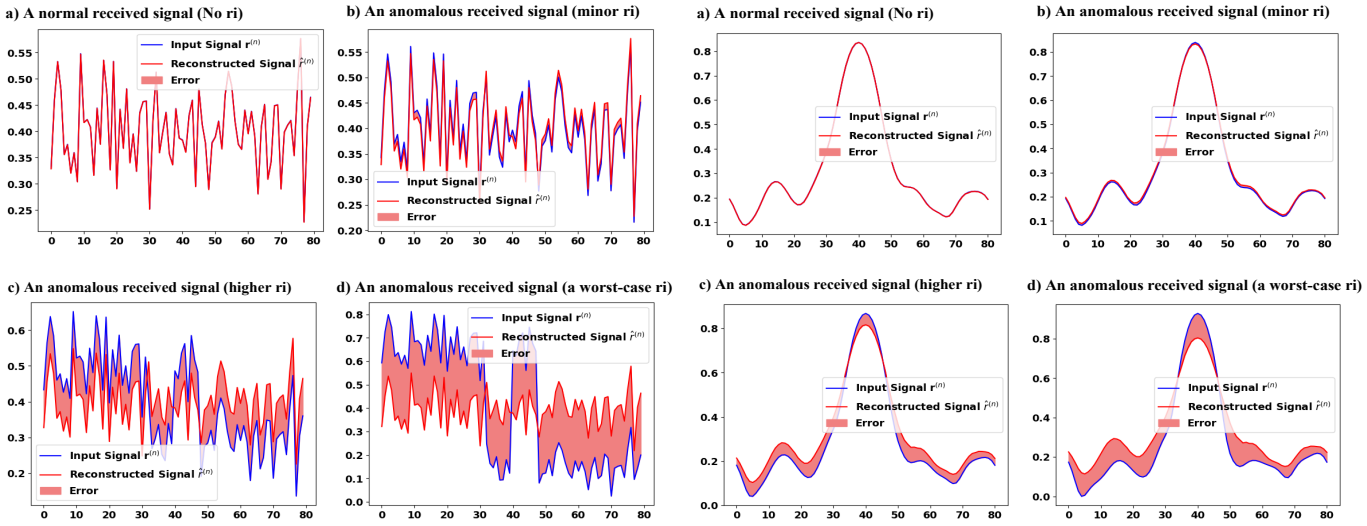

Fig. 6. Plots of normal and anomalous test examples from the $\mathbf{r_{Time}}$ & $\mathbf{r_{PSD}}$ input matrices, the reconstruction after it's encoded and decoded by the autoencoder, and the reconstruction error

$$\text{Encoding: } \tilde{\mathbf{z}}^{(\mathbf{n})} = \mathcal{F}_{\text{enc}}(\vec{r}_{\mathcal{M}}^{(n)}) \tag{8}$$

$$\text{Decoding: } \vec{r^*}_{\mathcal{M}}^{(n)} = \mathcal{F}_{\text{dec}}(\tilde{\mathbf{z}}^{(\mathbf{n})}) \tag{9}$$

where $\vec{r}_{\mathcal{M}}^{(n)}$ represents the input data, $\tilde{\mathbf{z}_\mathbf{n}}$ denotes the encoded representation or latent space, $\mathcal{F}_{\text{enc}}$ represents the encoder function that maps the input $\vec{r}_{\mathcal{M}}^{(n)}$ to the latent space $\tilde{\mathbf{z}}^{(\mathbf{n})}$. $\vec{r^*}_{\mathcal{M}}^{(n)}$ denotes the reconstructed output, $\mathcal{F}_{\text{dec}}$ represents the decoder function that maps the encoded representation $\tilde{\mathbf{z}}^{(\mathbf{n})}$ back to the reconstructed output $\vec{r^*}_{\mathcal{M}}^{(n)}$.

The goal of an autoencoder is to learn an efficient and meaningful representation of the input data by minimizing the reconstruction error between the original input ($\vec{r}_{\mathcal{M}}^{(n)}$) and the reconstructed output ($\vec{r^*}_{\mathcal{M}}^{(n)}$).

The interference problem is treated as an anomaly detection problem. We are testing using the actual received signal $\mathbf{r_{Time}}$, $\mathbf{r_{PSD}}$ matrices after normalizing each signal $\vec{r}_{\mathcal{M}}^{(n)}$.

IV. Experimental Results

A. Training the autoencoder model

Tensorflow and Keras frameworks are used to build the model in Python. The encoder and the decoder are specified using dense layers, and relu activation functions. We employ the sigmoid activation function in the output layer of the autoencoder, which enables us to directly compare the normalized input signal with the output data. The model is compiled with Mean Average Error (MAE) as the loss function, and Nesterov Implemented Adam as the optimizer. The weight and base parameters were updated using the **Train_data** set (only the 80% of the Normal_data segments), while the model evaluation is done using the full **Test_data** set. The input for the neural network (NN) is set to be the vector $\vec{r}_{\mathcal{M}}^{(n)}$ representing the normalized time or frequency signal at the n-th simulation Time-sample with a length of $\mathcal{M}$. The models converged in 20 epochs for both $\mathbf{r_{Time}}$, $\mathbf{r_{PSD}}$ input matrices as can be seen in Fig.5.

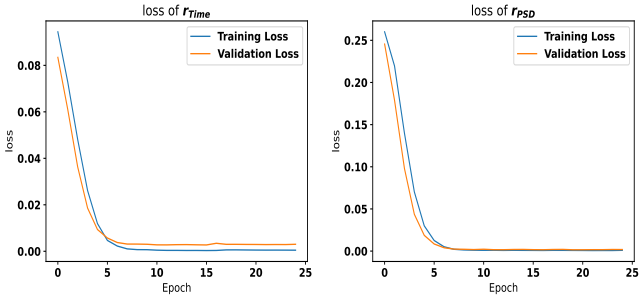

Fig. 5. Loss per epoch graph for $\mathbf{r_{Time}}$ Training Inputs in the left, and $\mathbf{r_{PSD}}$ Training Inputs in the right

Fig.6, shows different results from the model of normal and anomalous test examples from the $\mathbf{r_{Time}}$ & $\mathbf{r_{PSD}}$ training sets, the reconstruction after it is encoded and decoded by the autoencoder, and the reconstruction error.

B. Autoencoder interference detection performance

By thresholding, the reconstruction error, we can easily classify the anomalous receive signals $\vec{r}_{\mathcal{M}}^{(n)}$ by calculating whether the reconstruction loss is greater than a fixed decision threshold β. To set an initial threshold β_0, we will calculate the MAE for the normal segments from the training sets. Then, we will classify future examples as anomalous if the reconstruction error is higher than one standard deviation from the training sets. The initial threshold value is the summation of the standard deviation and means of the training losses. Hence,

- β_0 for $\mathbf{r_{Time}}$ training losses = 0.0004840
- β_0 for $\mathbf{r_{PSD}}$ training losses = 0.0006148

As shown in Table III, by varying the decision threshold manually, we can adjust the accuracy, precision, and recall of the classifier.

TABLE III
ADJUSTING DETECTION PERFORMANCE VARYING THE DECISION THRESHOLD β VALUES

$\mathbf{r_{Time}}$				
β	0.0004840	0.0005251	0.0005569	0.0005615
Accuracy	0.7466743	0.8363215	0.9491035	1.0
Precision	1.0	1.0	1.0	1.0
Recall	0.7337386	0.8279635	0.9465045	1.0
$\mathbf{r_{PSD}}$				
β	0.0006148	0.0006257	0.0006333	0.0006495
Accuracy	0.7460960	0.8432620	0.9670329	0.9994216
Precision	0.9991721	0.9992732	0.9993710	0.9993924
Recall	0.7337386	0.8358662	0.9659574	1.0

Lastly, we classify a received signal using the test sets as an anomaly if the reconstruction error is greater than the improved decision threshold value. The improved thresholds affect the detection performance as described in the confusion matrices shown in Fig.7 and Fig.8

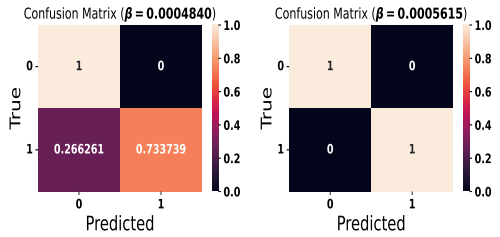

Fig. 7. Confusion matrix of the classificator for $\mathbf{r_{Time}}$ Test Inputs

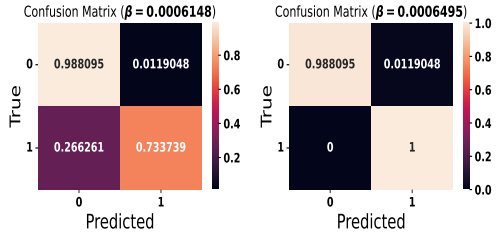

Fig. 8. Confusion matrix of the classificator for $\mathbf{r_{PSD}}$ Test Inputs

The Autoencoder model was able to reach an accuracy of 100% on the time domain $\mathbf{r_{Time}}$ data with a 0.0005615 threshold value. The same model achieved 99.9% on the frequency domain $\mathbf{r_{PSD}}$ data with a higher threshold value of 0.0006495. These results indicate that the model is able to detect the presence of different levels of interference signals in time-domain data representations more efficiently than its frequency-domain equivalents.

V. CONCLUSION

In this work, we address an emerging interference scenario, which corresponds to the NGSO-to-GSO downlink interference detection. For this, we proposed an autoencoder-based anomaly detector which has been tested in a realistic simulated environment. We have compared two different data input representations: the time-domain signals, and frequency-domain signals as power spectrum density PSD values. The proposed model was able to detect when the received signal $r(t)$ is affected by interference with good accuracy and less threshold value in its absolute time domain representations than the PSD representations. In our future work, we plan to improve the GSO-NGSO simulation by including more satellites and generating more interference scenarios. Furthermore, we will consider the effect of using different modulation schemes, and also improve the deep learning model.

REFERENCES

[1] A. C. Boley and M. Byers, "Satellite mega-constellations create risks in Low Earth Orbit, the atmosphere and on Earth," Scientific Rep., vol. 11, no. 1, May 2021.

[2] B. Al Homssi et al., "Next Generation Mega Satellite Networks for Access Equality: Opportunities, Challenges, and Performance," in IEEE Communications Magazine, vol. 60, no. 4, pp. 18-24, April 2022

[3] On-board spectrum monitoring',https://artes.esa.int/projects/board-spectrum-monitoringobsm, accessed May 2023

[4] H. Zhang, D. Ren, and F. Jiang, "A Beam Search-Based Channel Allocation Method for Interference Mitigation of NGSO Satellites with Multi-Beam Antennas," Aerospace, vol. 9, no. 4, p. 177, Mar. 2022

[5] S. K. Sharma, S. Chatzinotas and B. Ottersten, "In-line interference mitigation techniques for spectral coexistence of GEO and NGEO satellites", International Journal of Satellite Communications and Networking, vol. 34, pp. 11-39, 2016

[6] C. Wang, D. Bian, S. Shi, J. Xu, and G. Zhang, "A Novel Cognitive Satellite Network With GEO and LEO Broadband Systems in the Downlink Case," in IEEE Access, vol. 6, pp. 25987-26000, 2018

[7] M. Jalali, F. G. Ortiz-Gomez, E. Lagunas, S. Kisseleff, L. Emiliani and S. Chatzinotas, "Radio Regulation Compliance of NGSO Constellations' Interference towards GSO Ground Stations," 2022 IEEE 33rd Annual International Symposium on Personal, Indoor, and Mobile Radio Communications (PIMRC), Kyoto, Japan, 2022

[8] M. Á. Vázquez et al., "Machine Learning for Satellite Communications Operations," in IEEE Communications Magazine, vol. 59, no. 2, pp. 22-27, February 2021.

[9] F. Ortiz et al., "Onboard Processing in Satellite Communications Using AI Accelerators," Aerospace, vol. 10, no. 2, p. 101, Jan. 2023

[10] P. Henarejos, M. Á. Vázquez and A. I. Pérez-Neira, "Deep Learning for Experimental Hybrid Terrestrial and Satellite Interference Management," 2019 IEEE 20th International Workshop on Signal Processing Advances in Wireless Communications (SPAWC), Cannes, France, 2019

[11] L. Pellaco, N. Singh and J. Jaldén, "Spectrum prediction and interference detection for satellite communications," Advances in Communications Satellite Systems. Proceedings of the 37th International Communications Satellite Systems Conference (ICSSC-2019), Okinawa, Japan, 2019

[12] CelesTrak: Current GP Element Sets https://celestrak.org/NORAD/elements , accessed April 2023

[13] G. N. Watson , "A Treatise on the Theory of Bessel Functions," Cambridge University Press, 1922

[14] "Satellite frequency bands" https://www.esa.int/Applications/Telecommunications_Integrated_Applications/Satellite_frequency_bands.accessed May 2023 .

[15] "Application for Fixed Satellite Service by Space Exploration Holdings, LLC", SAT-LOA-20200526-00055 / SATLOA2020052600055, Filed By William Wiltshire https://fcc.report/IBFS/SAT-LOA-20200526-00055, accessed May 2023

[16] P. D. Welch, "The use of fast Fourier transforms for the estimation of power spectra: A method based on time averaging over short modified periodograms," IEEE Transactions on Audio and Electroacoustics, vol. 15, pp. 70-73, 1967

[17] Goodfellow, Y. Bengio and A. Courville, Deep Learning, Cambridge, MA, USA:MIT Press, 2016. Chapter 14, Autoencoders